Arch. Metall. Mater. **69** (2024), 3, 943-954

DOI: https://doi.org/10.24425/amm.2024.150914

M.A. OLOPADE[1], O.O. OYEBOLA[1], R.O. BALOGUN[1,3*], A.D. ADEWOYIN[2], A.B. ADEGBOYEGA[1]

IN-SILICO INVESTIGATION OF PHOTOVOLTAIC PERFORMANCE OF $MgXS_3$ (X = Ti AND Zr) CHALCOGENIDE PEROVSKITES COMPOUNDS

First-principles density functional formulation was used to explore the electronic and optical properties of magnesium chalcogenides sulfides, $MgXS_3$ (X = Ti and Zr), which compose of magnesium titanium sulfide, $MgTiS_3$, and magnesium zirconium sulfide, $MgZrS_3$. The lattice parameter calculations for $MgZrS_3$ yielded 9.19 Å, a bulk modulus of 170.6 GPa, and an equilibrium volume of 423.03 $Å^3$. In contrast, $MgTiS_3$ yielded 9.27 Å, a bulk modulus of 251.3 GPa, and an equilibrium volume of 117.06 3 $Å^3$. The computation gave a direct bandgap value for $MgTiS_3$ and $MgZrS_3$ of 1.1 eV and 1.3 eV, respectively. The dielectric constants of 38 and 32 were observed for the imaginary and real values for energy equivalents of 0.7 eV and 1.35 eV. The determined dielectric constants and energy values of the perovskite compounds were 70 and 1.35 eV respectively with their point of intersection also at this bandgap value. The efficiency of the compounds was calculated using the spectroscopic limited maximum efficiency (SLME) in order to ascertain their output as absorber materials. The findings show that $MgZrS_3$ had a higher efficiency value of 32.54% and $MgTiS_3$ with 29.45%. These compounds' computed properties point to the possibility of creating inexpensive, non-toxic absorber layer materials for use in solar cell development and other electronic applications.

Keywords: First-principle calculations; Chalcogenide; electronic materials; optical material; band gap; plane-wave pseudopotential method; SLME

1. Introduction

A number of optoelectronic, photonic, and energy technologies all heavily rely on the pursuit of technical improvement, particularly in the area of semiconductors. The predominant materials used in today's semiconductors, such as silicon, group III-V, and group II-VI, are typically built from a four-fold coordinated tetrahedral network of covalent bonds. Significant progress has been made in the development of semiconductors for solar cells, including Si, GaAs, $CuIn_xGa_{1x}Se_2$ (CIGS), and lead halide perovskite-based materials [1-3]. Investigations into metal chalcogenides have primarily centered on in-depth studies in recent years [4]. Greek word "chalcos" is where the word "chalcogenide" first appeared. A chalcogen element, such as S, Se, or Te, plus one of the group IVA or VA metallic ions are the main components of chalcogenides [5]. However, oxygen is not employed because of its extraordinary and significant chemistry and must be handled independently [6]. Chalcogenide is an amorphous or crystalline covalently bonded material with bandgaps between 0.0 and 3.5 eV. In a similar setting, they are highly different from common inorganic and opaque glasses, such silica or silicates, in that they are translucent in the infrared range. Compared to semiconducting or insulating materials, chalcogenide is far less studied because of its complicated structure, chemical makeup, and peculiar interatomic coordination. It is clear that the components of the three-solid form of the chalcogen, S, Se, and Te, have limited thermal stability. In order to create chalcogenides with special qualities in addition to the IVA and VA components of the group, scientists combined them with other elements [7]. These three elements' most prized and important trait is their inventive disposition, which is necessary to create new bonds and complexes [8]. Primary group metals and the transition-containing class of chalcogenide compounds exhibit valuable physical and chemical properties that are typically useful for use in a wide range of technological applications. Optical storage devices, thermoelectric devices, radiator detectors, nonlinear optics, thin-film electronics, solar energy conversion devices, catalysis, spintronics, and even superconductivity are a few examples [8]. There have been countless new technologies identified [9]. In contrast to the common perovskite lead

[1] UNIVERSITY OF LAGOS, FACULTY OF SCIENCE, DEPARTMENT OF PHYSICS, AKOKA, LAGOS, NIGERIA
[2] UNIVERSITY OF LAGOS, DISTANCE LEARNING INSTITUTE, AKOKA, LAGOS, NIGERIA
[3] SCHOOL OF SCIENCE AND TECHNOLOGY, PAN-ATLANTIC UNIVERSITY, IBEJU-LEKKI, LAGOS, NIGERIA
* Corresponding author: roluwanifemi@yahoo.com

halides, chalcogenides perovskites represent a significant class of promising, reliable, and less hazardous photovoltaic materials [10]. Recent research suggests that lead halide perovskites are not as ecologically friendly as chalcogenides perovskites in the ABX_3 form (X = S, Se, A, and B = metals with merely a total oxidation state of 6).

So far, a number of substances related to chalcogenide perovskite have been created. Nevertheless, it has been observed that the optimal form of the deformed perovskite for $CaZrS_3$, $CaHfS_3$, $BaZrS_3$, and $BaHfS_3$ with 3D connected corner-sharing BX_6 octahedra. It has been possible to experimentally manufacture other chalcogenide combinations, particularly from edge-sharing phases or isolated octahedra BX_6 (the purported "need-like" and "hexagonal" forms). Based on the absence of related octahedra in specific crystal composition directions, it is projected that such structures will exhibit additional localized conduction and edges of the valence band. This occurs mostly before heavy electrons and hole masses. In order to fit the deployment of solar cells, the $CaZrS_3$, $CaHfS_3$, $BaZrS_3$, and $BaHfS_3$ perovskites are anticipated from carrier mobility [11]. These proposals were based on the fact that the chalcogenide perovskites are less toxic, more common, and more environmentally friendly than the halide and oxide perovskites. In addition, chalcogenide perovskites outstanding optoelectronic properties made them ideal for use with pricey and commercially available tandem solar cells [12,14,15].

To create single-junction photovoltaic, several distorted perovskites with bandgaps of 1.75 eV for $BaZrS_3$, 1.0 eV for $CaTiS_3$, 1.2 eV for $CaHfSe_3$, and 1.3 eV for $CaZrSe_3$ are suitable, according to Sun et al. (2015). Perovskites are primarily semiconductors of negative charge carriers, with densities of between 10^{17} and 10^{21} cm^{-3}, according to the researcher's findings [16]. Chalcogenide perovskites have also been demonstrated to be promising materials that are useful in overcoming the long-term problem of halide perovskite instability and its dangerous nature based on their good optical absorption properties. Perera et al. (2019) sulphurated iron-oxide equivalents at high temperatures (2019). Several chalcogenide perovskites were made, and studies indicate that they have a projected band gap of 1.73-2.87 eV, subject to change. However, [17,18] properly predicted the optical direct bandgap range of 0.9-1.6 eV, with the latter using first-principle DFT formulations to show the optical electrons excitation of the x-ray diffraction spectrum for single-junction solar cell application.

For the solar applications, distorted values of α-$SrZrS_3$ (1.53 eV) and β-$SrZrS_3$ (2.13 eV) were used [19]. Various chalcogenides perovskites have been created recently with a focus on solar cells. Alkaline-earth metal chalcogenides [AECs], according to researchers, are a theoretical works are beneficial in microelectronics, catalytic processes, and in uses beyond solar cells [20]. These advantages sparked a great deal of theoretical and practical studies, which eventually resulted in the creation of bright devices [21-23].

Si, GaAs, and $CuInSe_2$ are currently the most popular solar-absorbing photovoltaic materials. Despite their accidental discovery, these materials have been steadily improved for cost-effectiveness and future study. For usage as sun absorbers in optoelectronic and solar cell applications, more than 135 000 materials are currently being carefully studied. The conventional and widely used Shockley and Queisser limit (S.Q.), which only considers the energy gap value of approximately 1.3 eV and disregards the transition of the electron migration between the conduction and valence band, leaves room for other crucial factors to precisely determine a better solar-absorber. The Spectroscopic Limited Maximum Efficiency (SLME) [24], which considered the absorption spectra, film thickness, and bandgap in addition to the S.Q. limit, performed better than the S.Q. limit. A range of materials, including perovskites [25-26], chalcogenides [27–28], straight band gap silicon crystals [29], and others [30], have been successfully treated with the SLME. Similar to this, I-III-VI_2 ternary semiconductors, such as the well-known Cu (In, Ga) $(S, Se)_2$ compounds, have frequently been used as absorber components to construct highly flexible and lightweight solar cells. Due to the high absorption coefficients of these compounds, it has been possible to develop affordable absorber layers that are ideal for deposition on flexible substrates [31]. The efficiency of CuIn $(S, Se)_2$ thin film solar cells recently reached a record high of 22.3 percent [32]. Moreover, CuIn $(S, Se)_2$ has been regarded as a good material for the top cell in tandem systems [33]. It has also been regarded as luminous solar concentrator based on quantum dots [34]. The quick succession of new efficiency records suggests that these applications still have the opportunity for development.

Few studies have been done on chalcogenide perovskites, despite the fact that there is literature accessible on the optical and electrical characteristics of oxides and halide metal perovskites [35–38]. Instead, perovskites made of halides and their oxide counterparts have received all of the attention from researchers. [39-41]. These advancements have demonstrated that chalcogenide perovskites have stronger photovoltaic properties than previously thought. Further investigation into the optical properties and theoretical electrical band structure of orthorhombic chalcogenide perovskite compounds was conducted [42-44].

This study examines the electronic and optical characteristics of the $MgXS_3$ (X = Ti and Zr) magnesium titanium and magnesium zirconium sulfides in response to the development on the photovoltaic effects of chalcogenide perovskites. DFT calculations on the electronic, optical, and structural (lattice parameter, bulk modulus, equilibrium volume) properties were carried out in this study using the QUANTUM ESPRESSO program. Band structure, real and imaginary dielectric constants, reflectance, energy-loss spectrum, absorption coefficient, optical conductivity, and SLME are among the electronic properties that have been estimated.

2. Computational methods

The $MgXS_3$ (X = Ti and Zr) structure has been studied using a first-principles approach within the Density Functional Theory (DFT) formalism [45-50], as implemented in the Quan-

tum Espresso Package [51-52]. In this research, the Projector Augmented Wave (PAW) method [53] was used in the package execution. The exchange-correlation function was calculated using the Generalized Gradient Approximation (GGA) of Perdew-Burke-Ernzerhof (PBE) [53]. The optimal cutoff energy was 40Ry after the converged energies between 10 Ry and 100 Ry were determined using the k-point converged value. The energy cutoff for the plane wave basis was set to 40Ry, and a 4×5×6 for $MgTiS_3$ and 6×7×9 for $MgZrS_3$ Monkhorst-Pack 30 (M.P.) mesh were used for sampling the first Brillouin zone. Electronic convergence is normally obtained when the energy difference between two electronic steps is smaller than 10^{-5} eV. Therefore, the structure is considered converged when the forces on the atoms are all below 10^{-3} eV/Å.

The Birch-Murnaghan equation of state was fitted to all the lattice parameters, as shown below.

$$P(V)=\frac{3B_o}{2}\left[\left(\frac{V_o}{V}\right)^{\frac{7}{3}}-\left(\frac{V_o}{V}\right)^{\frac{5}{3}}\right]\left\{1+\frac{3}{4}\left(B_o^{'}-4\right)\left[\left(\frac{V_o}{V}\right)^{\frac{2}{3}}-1\right]\right\} \quad (1)$$

The internal energy, $E(v)$ is found by integration of the pressure.

$$E(V)=E_o+\frac{9V_0B_o}{16}\left\{\left[\left(\frac{V_o}{V}\right)^{\frac{2}{3}}-1\right]^3 B_o^{'}+\left[\left(\frac{V_o}{V}\right)^{\frac{2}{3}}-1\right]^2\left[6-4\left(\frac{V_o}{V}\right)^{\frac{2}{3}}\right]\right\} \quad (2)$$

Where P is the pressure, V_o is the reference volume, V is the deformed volume, B_o is the bulk modulus, B_o is the derivative of the bulk modulus with respect to pressure.

The cell relaxation for atomic locations was carried out within the Broyden-Fletcher-Goldfarb-Shanno (BGFS) technique for a unit cell. Iterating until the lattice constants stay intact, the output of the variable-cell relaxation provided a new lattice constant that was then utilized for additional computations [54].

As a result, an extension of the HSE06 functional computation was carried out in order to accurately update the quasi-particle energies inside the HSE06 functional approximation. This is because an accurate band gap is crucial for determining the efficiency of solar absorbers. Thus, in the PAW structure, the semi-core electron would as well serve as a valence electron. The Kramers-Kronig connection was used to calculate the optical characteristics' dielectric constant [55] while the Kramers-Kronig (K.K.) formulations, which are mathematical tools for optical characteristics, were used to calculate the dielectric constants for the attributes [56].

$$\varepsilon_r=\varepsilon_1+i\varepsilon_2 \quad (3)$$

This equation is the sum of the real and imaginary part of the dielectric function, where ε_r is the dielectric function, $\varepsilon_1(\omega)$ is the real part of the dielectric function and ε_2 is the imaginary part of the dielectric function and ω is the angular velocity where

$$\varepsilon_1(\omega)=1+\frac{2}{\pi}\int_0^{\infty}\frac{\omega^1\varepsilon_2(\omega)\delta\omega^1}{\omega^1-\omega^2} \quad (4)$$

and,

$$\varepsilon_2(\omega)=\frac{-2}{\pi}\int_0^{\infty}\frac{\omega^1\varepsilon_2(\omega)\delta\omega^1}{\omega^1-\omega^2} \quad (5)$$

The efficiency of the solar absorbers was calculated using the spectroscopic limited maximum efficiency (SLME) for the materials. In the ideal scenario when the hole-electron pairs recombination process is radiative, Yu and Zunger's generalization of the detailed balancing efficiency limit of a *p-n* junction SC is applicable. The absorptivity, thickness, and recombination process of possible PV absorber materials are not taken into account in the SQ model; only their band gaps are considered [57]. The SLME method accounts for the non-radiative recombination (NRR), which is important for a material with an indirect fundamental band gap, by modelling the proportion of radiative recombination as a Boltzmann factor (i.e. Eq. (7)). For a material having an indirect fundamental band gap, this is significant. The SQ model's drawbacks were addressed by the SLME method by including the absorptivity (i.e., Eq. (8) [58].

$$\alpha(E)=\frac{4\pi E}{hc}\hat{k}(E) \quad (6)$$

h = the Planck's constant, c = light speed, and $\hat{K}(E)$ = extinction coefficient value.

$$\hat{K}(E)=\sqrt{\left(\frac{|\varepsilon(E)|-\varepsilon^{(1)}(E)}{2}\right)} \quad (7)$$

The photon absorptivity $\alpha(E)$ depends on both the optical absorption ccoefficient $\alpha(\omega)$ (Eq. (9)) and the absorber thickness L of the material. $\alpha(E)$ is expressed as:

$$\alpha(E)=1-e^{-2\alpha(\omega)L} \quad (8)$$

Eq. (8) calculates the photon absorptivity for solar absorber thickness L with reflective coated back [50].

$$\alpha(\omega)=\sqrt{2}\omega\left(\sqrt{\varepsilon_1(\omega)^2+\varepsilon_2(\omega)^2}-\varepsilon_1(\omega)\right)^{\frac{1}{2}} \quad (9)$$

The calculated maximum solar efficiency factor is calculated as

$$\eta=\frac{P_m}{P_{in}} \quad (10)$$

P_m = the maximum/output power density and P_{in} = Incident solar spectrum for input power.

The J-V characteristic determines the power density (max) of the solar cell.

$$J = J_{sc} - J_D \tag{11}$$

$$J_{sc} = e\int_0^{\infty} \alpha(E) I_{sun}(E) \delta E \tag{12}$$

$$J_D = J_0 \left(e^{\frac{q(V+JR_S)}{KT}} - 1 \right) \tag{13}$$

J = max current density, V = the absorber layer potential diff, k = heat energy constant, T = temperature of the device and e the charge quantity. J_{sc} = current density (short-circuit) and J_D = current density (reversed saturation). All other parameters were calculated from the absorptivity of materials $\alpha(E)$.

The radiative recombination fraction f_r is modelled using the Boltzmann factor:

$$f_r = e^{\frac{-E|_g^{da} - E|_g}{KT}} \tag{14}$$

Where E_g and E_g^{da} are respectively, the main and materials allowed bandgap value. The fill factor measurement is calculated using the equation below:

$$FF = \frac{P_{\max}}{V_{oc} J_{sc}} \tag{15}$$

The open-circuit voltage of the material is given as follows:

$$V_{OC} = \frac{KT}{q} \ln\left(\frac{J_{sc}}{J_0} + 1 \right) \tag{16}$$

and the maximum power for conversion and efficiency is given below:

$$P_{\max} = J_{sc} - J_0 \left(e^{\frac{eV}{KT}} - 1 \right) V \tag{17}$$

3. Results and discussion

3.1. Structural properties

The majority of a material's characteristics are dictated by its crystal structure. The arrangement of atoms with the lowest energy at a specific temperature and pressure is a stable crystal structure [59]. This analysis considered an orthorhombic phase of $CaZrS_3$ with a crystal structure similar to $BaZrS_3$ (space group Pnma (62) point group D^2h (mm)). Each Ca atom in the lattice, which is made up of deformed ZrS_6 corner-sharing octahedral as shown in Fig. 1, is centrally positioned in the spatial region defined by its neighbouring S and Zr atoms. Ca^{+2}, Zr^{+4}, and S^2 ions make up the ions.

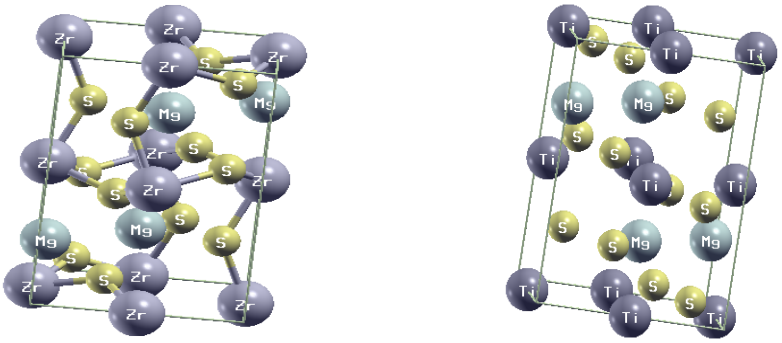

(a) (b)

Fig. 1. The CaZrS3-type crystallographic structures of (a) $MgZrS_3$ and (b) $MgTiS_3$

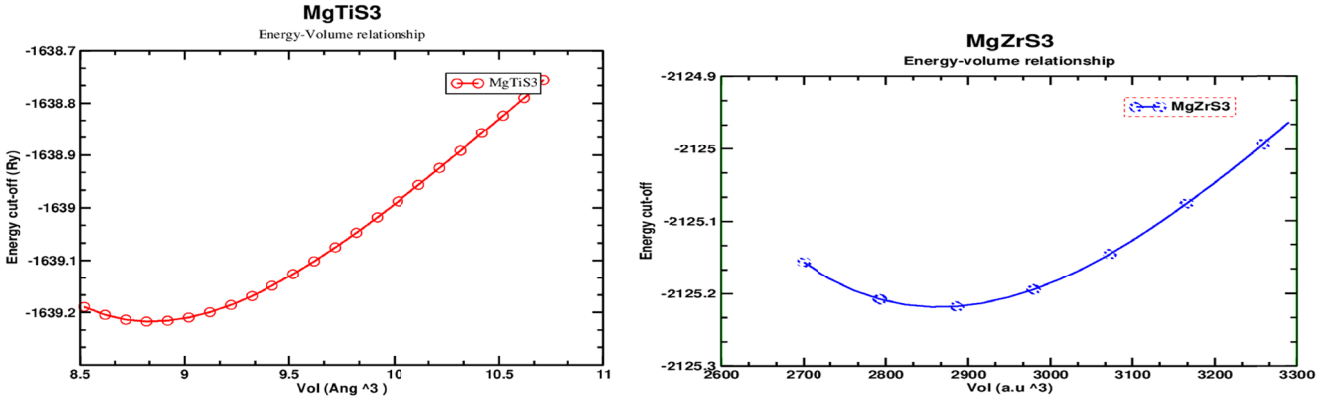

(a) (b)

Fig. 2. Optimization graphs for (a) $MgTiS_3$ and (b) $MgZrS_3$

As shown in Fig. 2. the convergent volumes of $MgTiS_3$ and $MgZrS_3$ are 9.27 and 9.19, respectively, on the plot of total energy against volume for $MgXS_3$. Recent theoretical and experimental findings for lattice volume and other relevant parameters are close matched by both volumes. More pertinent optimization points were therefore used for additional calculations.

The Birch-Murnaghan equation of state in Eqs. (1 & 2) were used to derive the structural lattice values of the two materials. These are shown in TABLE 1 (1). The equilibrium volume V_0 values were found to be 117.06Å^3 for $MgTiS_3$ and 424.04 Å^3 for $MgZrS_3$, as shown in TABLE 1. The volume discrepancies with other theoretical results may be because of the pseudopotential used because PBEsol [60] improves the structural properties of compound when compared to other pseudopotentials, which validates the improvement of generalized gradient approximation, GGA over local density approximation, LDA [61]. There is a good correlation between our results and those obtained by references [63,64] after analysis. The results of computations were then used to identify the additional physical characteristics of the materials. Hence, a list of additional approximated data from the Murnaghan equation of states is given in TABLE 1.

3.2. Electronic properties

The plane-wave pseudopotential method was used in this study's electronic calculations for the semiconductor materials $MgTiS_3$ and $MgZrS_3$. The resulting band structures of $MgTiS_3$ and $MgZrS_3$ are depicted in Figs. 3 and 4. The graph shows the relationship between wave-vector trajectories and energies between –5.0 and 4.0 eV. Further analysis of the two plots reveals that $MgTiS_3$ has a near direct bandgap at gamma point of 1.1 eV and $MgZrS_3$ has a direct bandgap at gamma point of 1.3 eV. The bandgap obtained in this study and those of [61,62], and [63] are in good agreement. The findings also support the notion that alkaline earth chalcogenides are advantageous materials for photovoltaic applications due to their potential for direct band gaps with high optical absorption coefficients that are comparable to those of traditional optoelectronic semiconductors like GaAs and their substantial band dispersion, which suggests good carrier mobility. Some chalcogenides in the phase, such as $SrZrS_3$, $BaZrSe_3$, and $SrHfSe_3$ [64], display more acceptable band gaps (1.0 eV-1.5 eV), which are identified as the promising materials for solar energy conversion. Furthermore, the results of our studies compare favourably with existing experimental and theoretical reports.

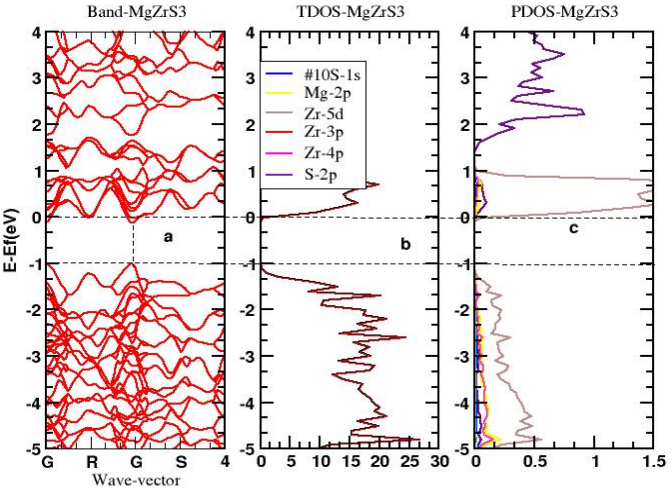

Fig 3. (a) Band Structure of $MgZrS_3$ (b) Total Density of states of $MgZrS_3$ (c) PDOS of $MgZrS_3$

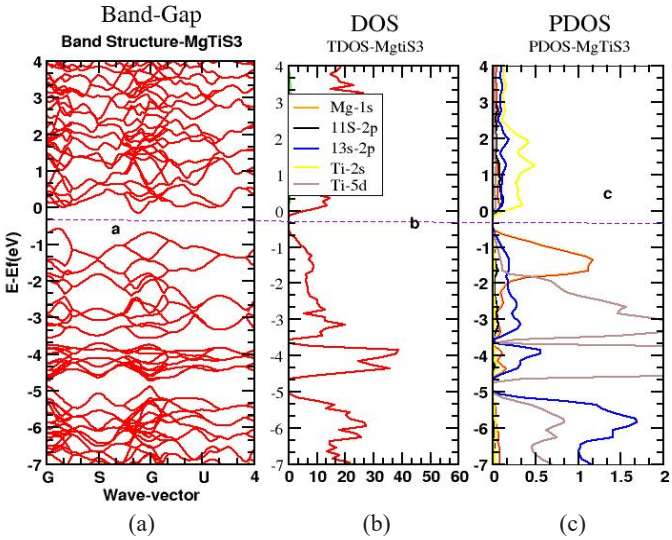

Fig. 4. (a) Band Structure $MgTiS_3$ (b) Total Density of states $MgTiS_3$ (c) PDOS of $MgTiS_3$

TABLE 1

Calculated lattice constant a_0 (Å), bulk modulus B, equilibrium volume V_0 (Å^3) and band gap E_g for $MgTiS_3$, $MgHfS_3$ and $MgZrS_3$ compared to other theoretical studies and experiment

Physical parameter	**$MgTiS_3$**	**$MgZrS_3$**	**$MgHfS_3$ [61]**	**Theory**	**$CaZrS_3$ [62]**	**$SrZrS_3$ [62]**	**$BaHfZr_1S_2$**	**Experiment [63]**
Lattice constant a_0 (Å)	9.27	9.19	9.59	10.077 [64]	9.66	9.85	10.022	9.98 [30]
Bulk modulus B (GPa)	251.3	170.6	78.9	—	—	—	74.28	
Volume V_0 (Å3)	117.06	424.09	439.53	511.059 [71]	450.80	480.63	501.2	441.89 [30]
Band gap E_g (eV)	1.1	1.3	1.43	0.9-1.6 [76], 1.0-1.75 [64], 1.12 [30]	1.17	1.18	3.96	1.73-1.85 [30], 0.99 [71]
Emin (Ry)	–517.07	–2125.22	–2470.2	—	—	—	–25873.04	
Tolerance factor	0.79	0.75	0.76	—	—	—	–0.953	

[71,64] Sun et al., 2015 [40] Wang et al., 2000 [76,6] Niu et al., 2018 [61] Balogun et al., 2021 [62] Liu et al., (2023). [63] Chami et al., (2021)

The chemical bond hybridization of Mg-2p, Zr-5d or Ti- 5d, and S-2p was dominant in the electronic structure of $MgZrS_3$ or $MgTiS_3$. The density of states, TDOS in Figs. 3 and 4 shows that the binding link is positioned inside the atoms closer to the Fermi energy level. The computed DOS and PDOS show the semiconductor nature of the materials. The bandgap estimate, based on the band structure, provided additional confirmation of the materials' conducting nature for solar applications. In the s, p, and d configurations, the atomic states of Mg, Ti, Zr, and S were carefully investigated.

Figs. 3 and 4 show that Ti-5d occupies the valence band region more frequently than Zr-5d occupies the open conduction band. This is because Zr-5d and Ti-5d have more energy; consequently, they inhabit different conductivity bands. Greater titanium doping would increase the material's energy level in contrast to Zr doping, which reduces the material's energy level because fewer electrons are occupied in the conduction bands. These increase the electron-hole recombination's use in solar energy. The materials are bonded chemically by covalent bonds with little ionicity, as evidenced by the clear overlap between the zirconium, sulfur, and magnesium equivalents of the DOS structures across the energy range. The high-symmetry locations, which some prior theoretical studies have overlooked, are also present in the first Brillouin zone. The wave-like characteristics of the band structures of magnesium zirconium and titanium sulfides were used to calculate the bandgap values.

3.3. Optical properties

The results of the optical investigation were utilized to establish the compounds' eligibility for usage in photovoltaic applications, including their absorption spectra, reflectivity, refractive index, dielectric function, and extinction coefficient. The parameters were plotted using Grace, which shows plot snippets that illustrate P.V. applications. A comparison of our findings with the theoretical and experimental results is shown in TABLE 2.

An explanation for the medium's optical behaviour at each photon energy is provided by the dielectric constant as follows:

$$\varepsilon = \varepsilon_1 + \varepsilon_2$$

The real component ε_1 is connected to the photon energy absorbed in the medium, whereas the imaginary part ε_2 is related to the behaviour of materials with electronic characteristics (band-gap structure) in terms of absorption [65-66]. The dielectric of the two materials are shown by the peaks in Fig. 5. The dielectric function of $MgTiS_3$ is at 71.5, as shown in TABLE 2. A value of 38 has the sharpest peak at 0.7 eV, and the imaginary ε_2. The value of 32 has the highest energy value of 1.35 eV. Altogether, these values make up the dielectric constant = 70 for $MgZrS_3$.

The energy variation for the two materials spans from 0.5 eV to 3 eV, showing that they can function well as semiconductors. These values are in good agreement with those of silicon and other perovskite materials, making them an alternative to silicon [67]. Also, the dielectric constant has a significant impact on solar cells' power conversion efficiency (PCE). A reduced coulombic interaction between weakly coupled electron-hole pairs will have less of an impact on charge-transfer states, and recombination involving mobile carriers will have less of an impact on radiative losses. According to our findings, $MgZrS_3$ has a higher dielectric constant value than $MgTiS_3$, making it the better material for solar cells. This compares well with GaAs, Silicon, and $BaZrS_3$ [68].

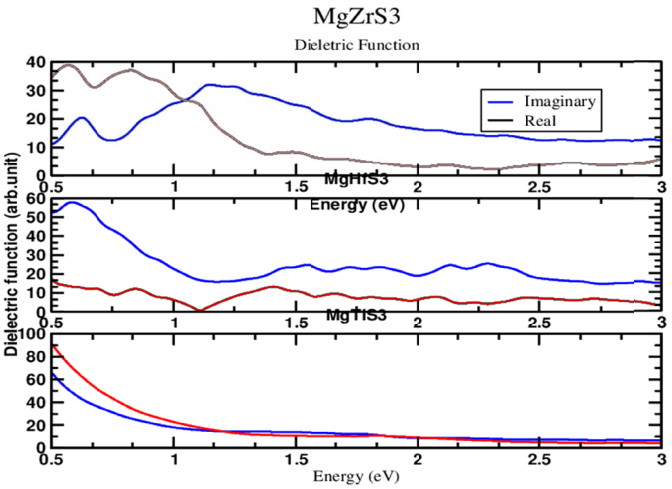

Fig. 5. Calculated Dielectric function (Real & Imaginary) of $MgTiS_3$ and $MgZrS_3$

The refractive index formula describes the determined absorption coefficient and refraction indices of the materials:

$$N(\omega) = n(\omega) + ik(\omega)$$

where $n(\omega)$ is the refractive index and $k(\omega)$ the extinction coefficient, as shown in Fig. 7. The refractive index is between the

TABLE 2

The calculated optical properties for $MgTiS_3$ and $MgZrS_3$

Materials	Dielectric	Refractive Index	Reflectivity	Absorption coefficient	Extinction coefficient
$MgZrS_3$	**R = 32, I = 38**	**6.8**	**0.75**	**5.02×10^8 m^{-1}**	**6.25**
$MgTiS_3$	**R = 17, I = 32**	**9.5**	**0.70**	**2.73×10^8 m^{-1}**	**3.25**
Si [30]	—	3.9	0.73	10^8 m^{-1}	0.03020
$BaTiS_3$ [17]	R = 60, I = 78	8.2	0.7	7×10^8 m^{-1}	5.5
GaAs	R = 24, I = 26	5.0	0.82	2.2×10^8 m^{-1}	4.2
$BaZrS_3$ [64]	R = 55.6, I = 19.6	5.7	0.6	5.93×10^7 m^{-1}	6.0
$MgHfS_3$ [51]	**R = 18, I = 58**	**6.11**	**0.52**	**5.12×10^8 m^{-1}**	**4.5**

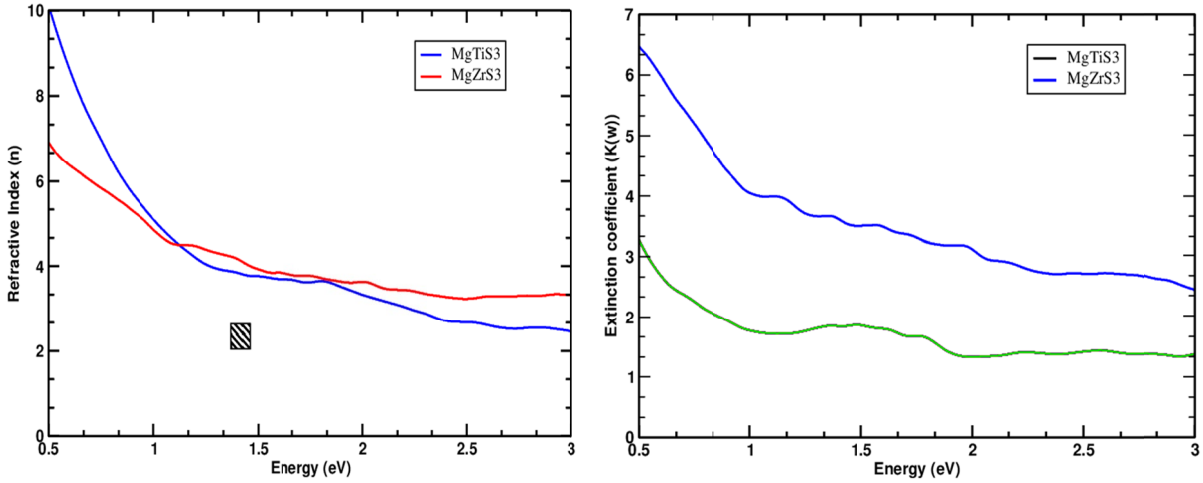

(a) (b)

Fig. 6. (a) Refractive indices of $MgTiS_3$ and $MgZrS_3$ (b) Extinction coefficient of $MgTiS_3$ and $MgZrS_3$

energy levels of 0.0eV and 3.0eV. Furthermore, the refractive index shows a proportional increase with energy, peaking at $n(\omega) = 10$ for $MgTiS_3$ within 0.7 eV and $n(\omega) = 6.3$ for $MgZrS_3$ within 0.60 eV. The decreasing curve for the two compounds achieves a constant decline at $n(\omega) = 3$, 1.3 eV energy area, which almost exactly matches their bandgaps. This fluctuation was brought about by a small number of electron oscillations [69], the curve in Fig. 7 shows that as energy levels rise photon transmission also rises.

The Extinction Coefficient $k(\omega)$ shows how solar radiation energy is diminished or attenuated as it travels through various materials. The attenuation coefficient of the substance is another name for the extinction value [60]. Prior to decline and stabilization, Fig. 7 shows that the extinction values peaked at roughly 6.5 for $MgZrS_3$ and 3.4 for $MgTiS_3$. In addition, their energy bandgaps of 1.1 eV for $MgTiS_3$ and 1.3 eV for the zirconium material roughly match the point of their stability. At the stability point, it was found that the extinction coefficient for both materials had a greater energy value of around 2.5 eV, allowing more incident solar energy to be absorbed by the material bandgap values. The production of solar absorber material will also result from the material becoming transparent as the radiant flux rises.

The strength of a material's ability to reflect radiation is measured by its reflectivity. Similarly, the reflectance factor is independent of the material's thickness. Thus, for $MgZrS_3$ and $MgTiS_3$, the reflectivity in Fig. 8. is at 0.72 and 0.68, respectively. This is contained inside the necessary 0.7 eV band gap for complete transmission. But before they settled for no reflectivity, the lowest troughs for titanium and the zirconium atom were detected at 0.41 and 0.52, respectively. As light energy exceeds the bandgap at the points of lower reflectivity, more radiation will be absorbed, ultimately leading to the development of materials with higher reflectivity for use in solar cells [64,70].

About the frequency or the wavelength of photon energy interaction with a material, the absorption coefficient quantifies how much radiation is absorbed by the substance. As shown in Fig. 7, the maximum for $MgZrS_3$ is at 4.8×10^8 and $MgTiS_3$ is at 2.8×10^8. The constant rise of the two materials was caused by photons transitioning from the occupied valence band (V.B); hole states to unoccupied hole states in the conduction band

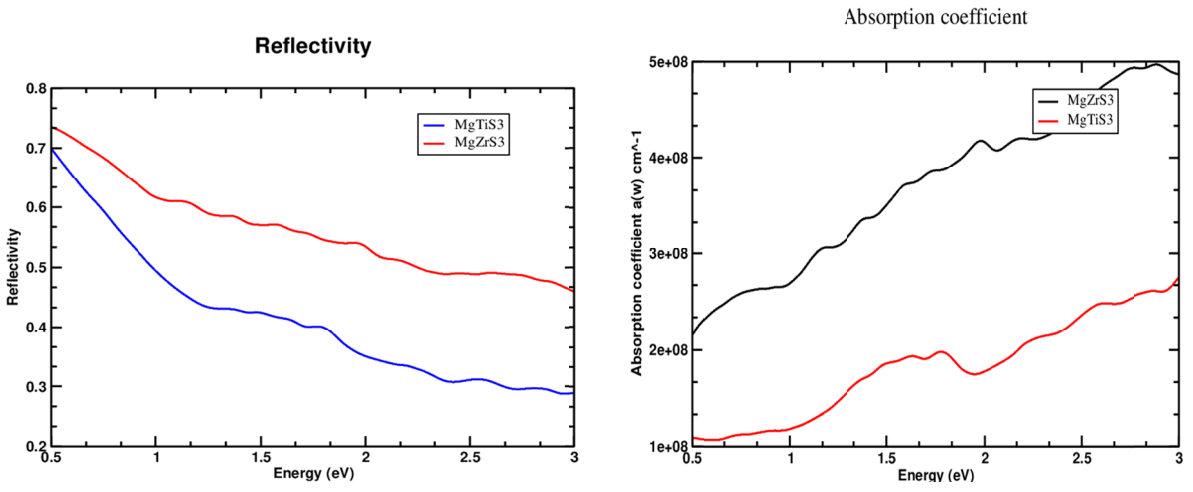

(a) (b)

Fig. 7. (a) Calculated Reflectivity of $MgTiS_3$ and $MgZrS_3$ (b) the Absorption coefficient of $MgTiS_3$ and $MgZrS_3$

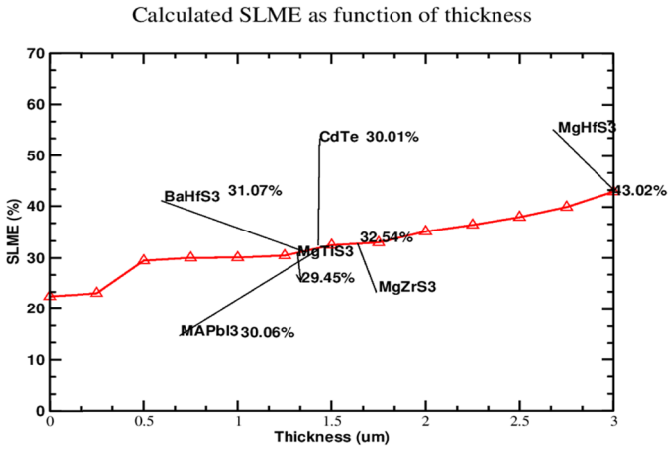

Fig. 8. Calculated SLME for $MgZrS_3$ and $MgTiS_3$

(C.B.) [71-73]. The relationship between the growing spectra and the increasing absorption coefficient is reciprocal [74]. The solar absorbers' SLME efficiency increased as a result of the zirconium atoms' growing absorption coefficient. This corresponds to the ultraviolet area of electromagnetic radiation, one of the regions with promising photovoltaic and optoelectronic applications [75-78].

3.4. SLME analysis of the Solar cell absorber for applications

The spectroscopic limited maximum efficiency (SLME) was employed to compute the potential of the solar absorbers of the materials. The data from the band structures and the materials' dielectric properties were utilized to estimate the photovoltaic potential. The SLME considers the film thickness when calculating the material efficiency. Thus, we achieved an acceptable and effective efficiency of between 1.5 µm and 3 µm thickness, with $MgZrS_3$ having 32.50% efficiency and $MgTiS_3$ having 29.45% respectively. The reference thickness would use the wavelength collected from the electronic, structural characteristics, and optical bandgaps to harness the penetration of visible light. Fig. 9 displays the computed findings and compares them. Additionally, the $MgTiS_3$ exhibits little to no variation in the primary and direct permitted bandgap. But this may be owing to the metallic character of titanium at Ti-5d orbitals, which is essential for non-radiative processes inside the material. Findings in this research are juxtaposed with perovskite materials because they are conceptually linked [79-82].

As shown in Fig. 9, the findings in this research outperformed the CdTe, barium and calcium zirconium sulfides, and traditional lead-halide perovskites in short-circuit current density to open-circuit voltage. It is inferred from the findings that the radiative penetration over the reflecting surface of the solar absorbers increases with increasing Hf, Zr, and Ti concentrations [83-84]. By allowing more radiant energy to pass over the surface of the solar cells, a high fill factor demonstrates the efficiency of the solar cell. In comparing silicon to other monocrystalline and thin-film solar cells made of CdTe and CIGS, the fill factor for silicon now gives about 80.

An examination of the implications of Figs. 10 and 11 indicate that $MgTiS_3$ and $MgZrS_3$ demonstrated the superior performance and unique solar absorbers for photovoltaic applications, which are superior to standard silicon, CdTe, and other polycrystalline cells [76-78]. Also, the variance of this research's efficiency demonstrates a consistent rise in the materials and matches the fill factor outcomes, which are intended to be proportionate.

4. Conclusion

This research has demonstrated that, for the first time, the optoelectronic characteristics of $MgXS_3$ can be investigated utilizing the DFT approach of the plane-wave pseudopotential method. The properties of the ground state lattice parameters were established. The values of specific chosen actual and theoretical chalcogenides and our computed results are similar. The research also discovered that the semiconductor materials have direct band gaps of 1.1 eV for $MgTiS_3$ and 1.3 eV for $MgZrS_3$ at their gamma point. In addition, the compounds' refractive indices, reflectivity, extinction coefficients, absorption coefficients, and dielectric function responses were calculated. The materials' high absorption spectra coefficient and reflectivity values explain why they help construct solar cells and

TABLE 3

The calculated factors affecting the efficiency of the photovoltaic application. fractional loss of radiation *Fr*, short-circuit current density J_{sc}, efficiency η, open-circuit voltage V_{oc}, fill factor *FF*, maximum input voltage V_{max} and maximum power P_{max}

Compounds	*Fr*	P_{max}	J_{sc} (mA/cm^2)	V_{oc} (V)	J_{mpp} (mA/cm^2)	V_{mpp} (V)	η (%)	*FF*
$MgHfS_3$	**1**	**42.55**	**16.36**	**2.75**	**16.16**	**2.55**	**43.02**	**93.50**
$MgZrS_3$	**1**	**32.55**	**27.70**	**1.16**	**27.50**	**1.36**	**32.50**	**86.67**
$MgTiS_3$	**1**	**29.45**	**24.34**	**1.21**	**24.54**	**1.24**	**29.45**	**80.64**
$BaHf_{1-x}Zr_xS_3$	1	22.46	14.73	1.65	14.50	1.55	22.45	92.18
$BaZrS_3$	1	30.86	27.19	1.26	26.61	1.16	30.45	90.30
CdTe	1	30.07	27.82	1.20	27.20	1.10	30.01	89.94
$Ca_2Zr_2S_7$			16.10	1.63			23.01	
$MAPbI_3$			25.27	1.31			30.06	91.00

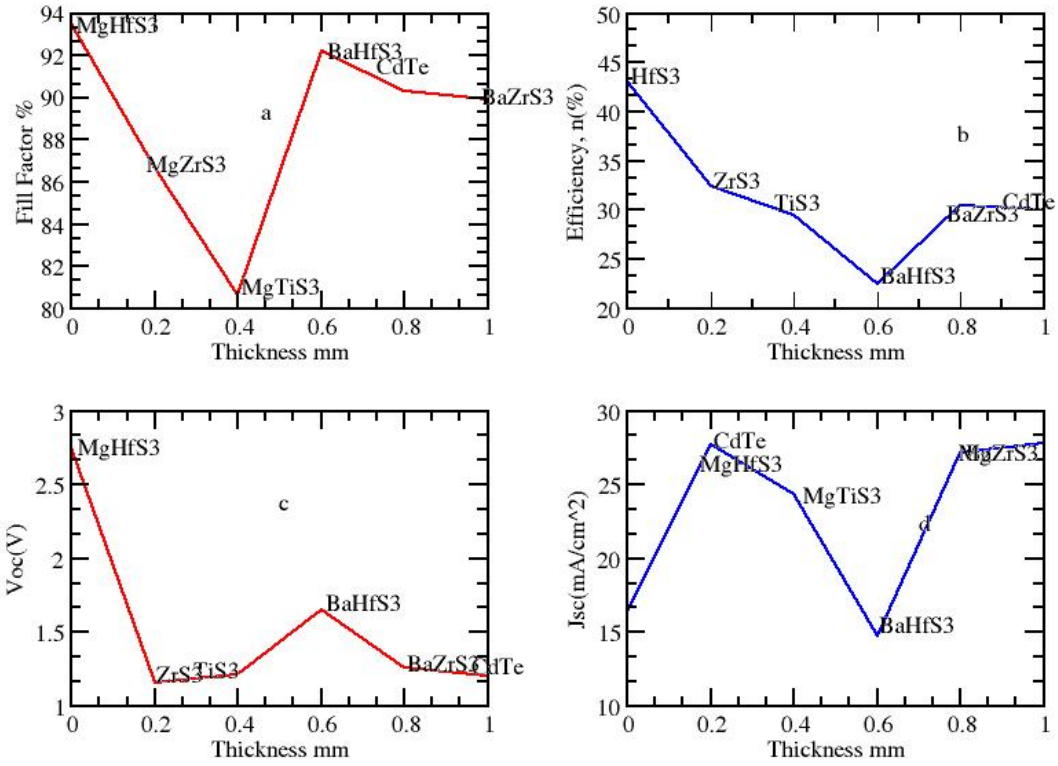

Fig 9. (a) Fill factor- thickness relationship of solar cells (b) Efficiency-thickness variations of solar cells (c) Open-circuit voltage thickness relationship of solar cells (d) Current density thickness variations of solar cells

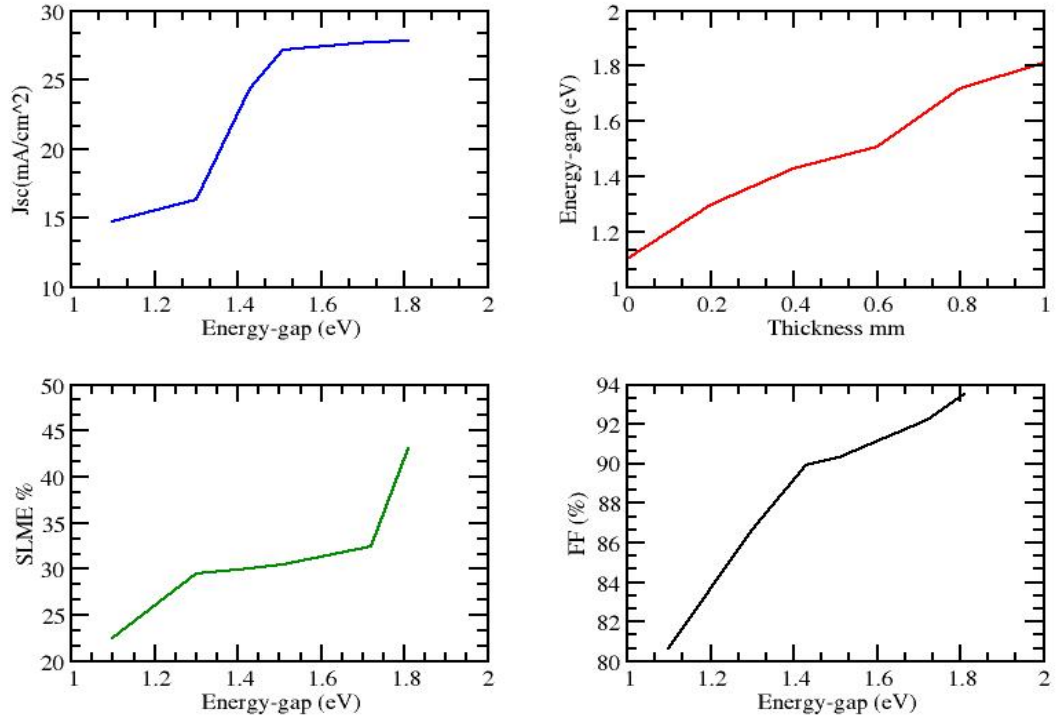

Fig.10. (a) Energy gap – current density variations of solar cells (b) Energy gap-thickness variations of solar cells (c) SLME variation with energy-gap of solar cells (d) Maximum Power-Fill factor relationship for solar cell

optoelectronic devices. Moreover, the potentials of the materials' solar absorbers were calculated using the spectroscopic limited maximum efficiency (SLME), which further show that $MgZrS_3$ has a higher efficiency value of 32.54% when compared to $MgTiS_3$ with a value of 29.45%. Fundamentally, this research yields optical results that are comparable to [32]. It therefore serves as a model for further theoretical and experimental studies on metal chalcogenides. For any upcoming study, the materials are affordable, non-toxic, effective solar absorbers, and abundant.

Authorship

All individuals who meet the requirements for authorship are listed as authors. Each author attests that they contributed sufficiently to the work and also assume responsibility for its content, including conception, design, analysis, writing, or manuscript revision. Additionally, each contributor attests that no other publication has received or will get this material or any material identical to it. (M. A. Olopade conceptualized, Computed, wrote, and analyzed the data; O.O. Oyebola revised the manuscript; R. O. Balogun assisted in Computation, data interpretation and manuscript editing; A.D. Adewoyin assisted in writing and data analysis and A.B, Adegboyega assisted with data analysis).

Acknowledgments

The authors are grateful to the Head of the University of Lagos' Physics Department and Basic Science Unit, Pan-Atlantic University for their academic and moral support.

REFERENCES

[1] M.A. Green, Prog. Photovoltaics **20**, 472-76 (2012). DOI: https://doi.org/10.1002/pip.1147

[2] K. Yoshikawa, H. Kawasaki, W. Yoshida, T. Irie, K. Konishi, K. Nakano, T. Uto, D. Adachi, M. Kanematsu, H. Uzu, K. Yamamoto, Nat. Energy **2**, 17032 (2017). DOI: https://doi.org/10.1038/nenergy.2017.32

[3] H.J. Snaith, Nat. Mater. **17**, 372-376 (2018). DOI: https://doi.org/10.1038/s41563-018-0071-z

[4] T. Sato, S. Takagi, S. Deledda, B.C. Hauback, S. Orimo, Extending the applicability of the Goldschmidt tolerance factor to arbitrary ionic compounds. Sci. Rep. **6** ,23592 (2016). [CrossRef]

[5] C.-S Lee, K.M. Kleinke, H. Kleinke, Synthesis, structure, and electronic and physical properties of the two SrZrS3 modifications. Solid State Sci. **7**, 1049-1054 (2005). [CrossRef]

[6] S. Hasan, P. Adhikari, K.Baral, W.-Y. Ching, Conspicuous interatomic bonding in chalcogenide crystals and implications on electronic, optical, and elastic properties. AIP Adv. **10**, 075216 (2020). [CrossRef]

[7] M.G. Kanatzidis Chalcogenides: Solid-State Chemistry Based in part on the article Chalcogenides: Solid State Chemistry by Patricia M. Keane which appeared in the Encyclopedia of Inorganic Chemistry, First Edition. In Encyclopedia of Inorganic Chemistry; John Wiley & Sons, Ltd.: Chichester, UK, pp. 1-39 (2006).

[8] N.P. Papoh, Introductory Chapter: Chalcogen Chemistry-The Footprint into New Materials Development. In Chalcogen Chemistry; Intech Open: London, UK, pp. 1-7 (2018).

[9] A. Nijamudheen, A.V. Akimov, Criticality of Symmetry in Rational Design of Chalcogenide Perovskites. J. Phys. Chem. Lett. **9**, 248-257 (2018). [CrossRef]

[10] W.;Meng, B. Saparov, F. Hong, J.Wang, D.B. Mitzi, Y. Yan, Alloying and Defect Control within Chalcogenide Perovskites for Optimized Photovoltaic Application. Chem. Mater. **28**, 821-829 (2016). [CrossRef]

[11] X.-K. Liu, F. Gao, Organic–Inorganic Hybrid Ruddlesden–Popper Perovskites: An Emerging Paradigm for High-Performance Light-Emitting Diodes. J. Phys. Chem. Lett. **9**, 2251-2258 (2018). [CrossRef]

[12] R. Nechache, C. Harnagea, S. Li, W. Huang, W. Cardenas, J. Chakrabartty, F. Rosei, Bandgap tuning of Multiferroic Oxide Solar Cells. Nat. Photonics **9**, 61 (2001).

[13] Z. Fan, K. Sun, J. Wang, Perovskites for Photovoltaics: A Combined Review of Organic−Inorganic Halide Perovskites and Ferroelectric Oxide Perovskites. J. Mater. Chem. A. **3**, 18809-18828 (2015).

[14] W. Meng, B. Saparov, F. Hong, J. Wang, D.B. Mitzi, Y. Yan, Alloying and Defect Control within Chalcogenide Perovskites for Optimized Photovoltaic Application Alloying and Defect Control within Chalcogenide Perovskites for Optimized Photovoltaic Application. Chem. Mater. **283**, 821-829 (2016).

[15] R. Pandey, S. Sivaraman, Spectroscopic properties of defects in alkaline-earth sulfides. J. Phys. Chem. Solids. **52**, 1, 211-225 (1991).

[16] S. Niu, J. Milam-Guerrero, B.C. Melot, Thermal stability study of transition metal perovskite sulfides. J. Mater. Res. **24**, 4135-4143 (2018).

[17] S. Asano, N. Yamashita, Y. Nakao, Luminescence of the Pb2+ -ion dimer center in CaS and CaSe phosphors. phys. status solidi (b). **89**, 2, 663-673 (1978).

[18] X. Wei, H. Hui, C. Zhao, C. Deng, M. Han, Z. Yu, A. Sheng, P. Roy, A. Chen, J. Lin, Realization of $BaZrS_3$ chalcogenide perovskite thin films for optoelectronics. Nano Energy **68**, 104317 (2020).

[19] S. Perera, H. Hui, C. Zhao, H. Xue, F. Sun, C. Deng, N. Gross, C. Milleville, X. Xu, D.F. Watson, B. Weinstein, Y.Y. Sun, S. Zhang, H. Zeng, Chalcogenide perovskites – an emerging class of ionic semiconductors. Nano Energy **22**, 129-135 (2016)

[20] M. Ju, J. Dai, L. Ma, X. C. Zeng, Perovskite Chalcogenides with Optimal Bandgap and Desired Optical Absorption for Photovoltaic Devices. Adv. Energy Mater. **8**, 2-8 (2017).

[21] A. Jain, S.P. Ong, G. Hautier, W. Chen, W.D. Richards, S. Dacek, S. Cholia, D. Gunter, D. Skinner, G. Ceder , K.A. Persson, APL Mater. **1**, 011002 (2013).

[22] W. Shockley, H.J. Queisser, J. Appl. Phys. **32**, 510 (1961).

[23] L. Yu, A. Zunger, Phys. Rev. Lett. **108**, 068701 (2012).

[24] W.-J. Yin, T. Shi, Y. Yan, Adv. Mater. **26**, 4653-4658 (2014).

[25] W.-J. Yin, J.-H. Yang, J. Kang, Y. Yan , S.-H. Wei, J. Mater. Chem. A. **3**, 8926-8942 (2015).

[26] W.-J. Yin, T. Shi, Y. Yan, J. Phys. Chem. C. **119**, 5253-5264 (2015).

[27] W. Meng, B. Saparov, F. Hong, J. Wang, D.B. Mitzi, Y. Yan, Chem. Mater. **28**, 821-829 (2016).

[28] F. Hong,W. Lin,W. Meng, Y. Yan, Phys. Chem. Chem. Phys. **18**, 4828-4834 (2016).

[29] N. Sarmadian, R. Saniz, B. Partoens, D. Lamoen, Submitted for publication, arXiv:1605.05842.

[30] I.-H. Lee, J. Lee, Y.J. Oh, S. Kim, K. J. Chang, Phys. Rev. B **90**, 115209 (2014).

[31] Y.J. Oh, I.-H. Lee, S. Kim, J. Lee , K.J. Chang, Sci. Rep. **5**, 18086 (2015).

[32] L. Yu, R.S. Kokenyesi, D.A. Keszler, A. Zunger, Adv. Energy Mater. **3**, 43-48 (2012).

[33] T. Yokoyama, F. Oba, A. Seko, H. Hayashi, Y. Nose, I. Tanaka, Appl. Phys. Express **6**, 061201 (2013).

[34] J. Heo, R. Ravichandran, C.F. Reidy, J. Tate, J.F. Wager, D.A. Keszler, Adv. Energy Mater. **5**, 1401506 (2014).

[35] X. Huang, T.R. Paudel, S. Dong, E.Y. Tsymbal, Phys. Rev. B **92**, 125201 (2015).

[36] P. Reinhard, A. Chirila, P. Blosch, F. Pianezzi, S. Nishiwaki, S. Buecheler, A.N. Tiwari, IEEE J. Photovolt. **3**, 572-580 (2013).

[37] Solar Frontier Achieves World Record Thin-Film Solar Cell Efficiency: 22.3%., Retrieved March **10**, (2016) from www.solar frontier.com/eng/news/2015/C051171.

[38] G. Cheek, F. Yang, H. Lee, 2013 IEEE 39th Photovoltaic Specialists Conference (PVSC), 2013.

[39] Y. Peng, Q. Sun, H. Chen, W. J. Yin, Disparity of the Nature of the Band Gap between Halide and Chalcogenide Single Perovskites for Solar Cell Absorbers. J. Phys. Chem. Lett. **10**, 4566-4570 (2019).

[40] M.W. Wang, M.C. Phillips, J.F. Swenberg, E.T. Yu, J.O. McCaldin, T.C. McGill, n-CdSe/p-ZnTe based wide bandgap light emitters: Numerical simulation and design. J. Appl. Phys. **73**, 9, 4660-4668 (1993).

[41] P. Gao, M. Grätzel, M.K. Nazeeruddin, Organohalide Lead Perovskites for Photovoltaic Applications. Energy Environ. Sci. **7**, 2448-2463 (2014).

[42] J. He, C. Franchini, J.M. Rondinelli, Ferroelectric Oxides with Strong Visible-Light Absorption from Charge Ordering. Chem. Mater. **29**, 2445-2451 (2017).

[43] C. Paillard, X. Bai, I.C. Infante, M. Guennou, G. Geneste, M. Alexe, J. Kreisel, B. Dkhil, Photovoltaics with Ferroelectrics: Current Status and Beyond. Adv. Mater. **28**, (33), 5153-5168 (2016).

[44] A. Swarnkar, V.K. Ravi, A. Nag, Beyond Colloidal Cesium Lead Halide Perovskite Nanocrystals: Analogous Metal Halides and Doping. ACS Energy Lett. **2**, 1089-1098 (2017).

[45] M.V. Kovalenko, L. Protesescu, M.I. Bodnarchuk, Properties and Potential Optoelectronic Applications of Lead Halide Perovskite Nanocrystals. Science **358**, 745-750 (2017).

[46] Q. Xu, D. Yang, J. Lv, Y.Y. Sun, L. Zhang, Perovskite Solar Absorbers: Materials by Design. Small Methods **2**, 1700316 (2018).

[47] V.K. Ravi, N. Singhal, A. Nag, Initiation and Future Prospects of Colloidal Metal Halide Double-Perovskite Nanocrystals: Cs_2AgBiX_6 (X = Cl, Br, I). J. Mater. Chem. A **6**, 21666-21675 (2018).

[48] W. Kohn, P. Hohenberg, Phys. Rev. B **136**, 864 (1964).

[49] W. Kohn, L.J. Sham, Phys. Rev. **140**, 1133 (1965).

[50] M. Born, R. Oppenheimer, Ann. Phys. **389**, 457 (1927).

[51] P. Giannozzi et al., J. Phys.:Condens. Matter. **29**, 465901 (2017). http://www.quantum-espresso.org/quote

[52] S. Baroni, S. de Gironcoli, A. Dal Corso, P. Giannozzi, Rev. Mod. Phys. **73**, 515 (2001).

[53] S. Baroni, P. Giannozzi, E. Isaev, Rev. Mineral. Geochem. **71**, 39 (2010).

[54] W.E. Pickett, Comput. Phys. Rep. **9**, 115 (1989).

[55] A. Kokalj, J. Mol. Graph. Model. **17**, 176-179 (1999). Code available from http://www.xcrysden.org/]

[56] X. C. Liu, R. Hong, C. Tian, Tolerance factor and the stability discussion of ABO_3-type ilmenite". Journal of Materials Science: Materials in Electronics **20** (4), 323-327 (2008).

[57] W. Shockley, H.J. Queisser, J. Appl. Phys. **32**, 510-519 (1961),

[58] L. Yu, A. Zunger, Phys. Rev. Lett. **108**, 068701 (2012).

[59] I. Sadeghi, K. Ye, M. Xu, Y. Li, J.M. LeBeau, R. Jaramillo, Adv. Funct. Mater. **31**, 2105563 (2021).
DOI: https://doi.org/10.1002/adfm.202105563

[60] K. Kuhar, A. Crovetto, M. Pandey, K.S. Thygesen, B. Seger, P.C. K. Vesborg, O. Hansen, I. Chorkendorff, K.W. Jacobsen, Sulfide Perovskites for Solar Energy Conversion Applications: Computational Screening and Synthesis of the Selected Compound $LaYS_3$. Energy Environ. Sci. **10**, 2579-2593 (2017).

[61] R.O. Balogun, M.A. Olopade, O.O. Oyebola, A.D. Adewoyin, First-principle calculations to investigate structural, electronic and optical properties of $MgHfS_3$. Materials Science and Engineering B: Solid-State Materials for Advanced Technology **273**, 115405. (2021).

[62] D. Liu, H. Zeng, H. Peng, R. Sa, Phys. Chem. Chem. Phys. (2023). DOI: https://doi.org/10.1039/D3CP01522J

[63] R. Chamia, A. Lekdadrib, L.H. Omari, E.K. Hlil, M. Chafia, Investigation of the photovoltaic properties of $BaHf_{1-x}Zr_xS_{3(x<-1)}$ Chalcogenide Perovskites using First Principle Calculations. Materials Today Energy (2021).
DOI: https://doi.org/10.1016/j.mtener.2021.100689

[64] S.J. Adjogri, E.L. Meyer, Chalcogenide Perovskites and Perovskite-Based Chalcohalide as Photoabsorbers: A Study of Their Properties, and Potential Photovoltaic Applications. Materials **14**, 7857 (2021). DOI: https://doi.org/10.3390/ma14247857

[65] D. Li, F. Ling, Z. Zhu, X. Zhang, Theoretical structural electronic and optical properties of $Cu_2CdGeSe_4$. Physica B. **406**, 3299 (2011).

[66] S. Niu, H. Huyan, Y. Liu, M. Yeung, K. Ye, L. Blankemeier, T. Orvis, D. Sarkar, D.J. Singh, R. Kapadia, J. Ravichandran, Adv. Mater. **29**, 1604733 (2017).

[67] N.A. Moroz, C. Bauer, L. Williams, A. Olvera, J. Casamento, A.A. Page, T.P. Bailey, A. Weiland, S.S. Stoyko, E. Kioupakis, C. Uher, J.A. Aitken, P.F.P. Poudeu, Inorg. Chem. **57**, 7402-7411 (2018).

[68] M. Ong, D.M. Guzman, Q. Campbell, I. Dabo, R.A. Jishi, J. Appl. Phys. **125**, 235702 (2019).

[69] A. Dolgonos, T.O. Mason, K.R. Poeppelmeier, Direct optical band gap measurement in polycrystalline semiconductors: A critical look at the Tauc method. J. Solid State Chem. **240**, 43-48 (2016).

[70] Z. Xiao, Y. Zhou, H. Hosono, T. Kamiya, N.P. Padture, Bandgap Optimization of Perovskite Semiconductors for Photovoltaic Applications. Chem.-Eur. J. **24**, 2305-2316 (2018).

[71] M.S. Dresselhaus, Solid State Phys. Part II Opt. Propert. Solid. **23**, 56-66(2001).

[72] E. Osei-Agyemang, G. Balasubramanian, Understanding the Extremely Poor Lattice Thermal Transport in Chalcogenide Perovskite $BaZrS_3$. ACS Applied Energy Materials **3** (1), 1139-1144 (2020).

[73] H.J. Monkhorst, J.D. Pack, Phys. Rev. B **13**, 5188 (1976).

[74] J. Hwang, R.R. Rao, L. Giordano, Y. Katayama, Y. Yu, Y. Shao-Horn, Perovskites in Catalysis and Electrocatalysis. Science **358**, 751-756 (2017).

[75] J.P. Perdew, K. Burke, M. Ernzerhof, Phys. Rev. Lett. **77**, 3865-3868 (1996).

[76] J.P. Perdew, A. Ruzsinszky, G.I. Csonka, O.A. Vydrov, G.E. Scuseria, L.A. Constantin, X. Zhou, K. Burke, Phys. Rev. Lett. **100**, 136406 (2008).

[77] A. Jodlowski, D. Rodríguez-Padró, R. Luque, G. de Miguel, Alternative Perovskites for Photovoltaics. Adv. Energy Mater. **8**, 1703120 (2018).

[78] M.D. Segall, P.J.D. Lindan, M.J. Probert, C.J. Pickard, P.J. Hasnip, S.J. Clark, M.C. Payne, J. Phys.: Condens. Matter. **14**, 2717 (2002).

[79] Y. Sun, M.L. Agiorgousis, P. Zhang, S. Zhang, Chalcogenide Perovskites for Photovoltaics. Nano Lett. **15**, 581-585 (2015).

[80] F.D. Murnaghan, The compressibility of media under extreme pressures. Proc.Natl. Acad. Sci. U.S.A. **30**, 244 (1944).

[81] P. Giannozzi, S. Baroni, N. Bonini, M. Calandra, R. Car, C. Cavazzoni, D. Ceresoli, G.L. Chiarotti, M. Cococcioni, I. Dabo, A.D. Corso, S. de Gironcoli, S. Fabris, G. Fratesi, R. Gebauer, U. Gerstmann, C. Gougoussis, A. Kokalj, M. Lazzeri, L. Martin-Samos, N. Marzari, F. Mauri, R. Mazzarello, S. Paolini, A. Pasquarello, L. Paulatto, C. Sbraccia, S. Scandolo, G. Sclauzero, A.P. Seitsonen, A. Smogunov, P. Umari, R.M. Wentzcovitch, J. Phys. Condens. Matter. **21**, 395502 (2009).

[82] H.A. Kramers, AttiCongr. Intern. Fisicas Trans. Volta Centenary-Cong. **22,** 545–557 (1927).

[83] Y. Cui, G. Wang, D. Pan, Synthesis and Photoresponse of Novel Cu_2CdSnS_4 Semiconductor Nanorods, J. Mater. Chem. **22**, 12471-7 (2012).

[84] Y.Y. Sun, M.L. Agiorgousis, P. Zhang, S. Zhang, Nano Lett. **15**, 581 (2015).

[85] W. Zachariasen, Über die Kristallstruktur des Magnesium tellurids. Z. Phys. Chem., Stoechiom. Verwandtschaftsl. **128**, 417 (1927).

[86] H.G. Zimmer, H. Winze , K. Syassen, High- pressure phase transitions in CaTe and SrTe. Phys. Rev. B. **32**, 4066-4070 (1985).